Evolution of the Cenozoic Tarim Basin by flexural subsidence and sediment ponding: insights from quantitative basin modelling

Evolution of the Cenozoic Tarim Basin by flexural subsidence and sediment ponding: insights from quantitative basin modelling

Chao Li[a], ShengLi Wang[a*], Mark Naylor[b], Hugh Sinclair[b], LiangShu Wang[a**]

[a]State Key Laboratory for Mineral Deposits Research, Department of Earth Sciences, Nanjing University, Nanjing, China

[b]School of GeoSciences, University of Edinburgh, Edinburgh, UK

First author: Chao Li

Email: dabaoixiaobao@gmail.com

*Corresponding author: ShengLi Wang

Postal address: No. 163 Xianlin Avenue, Nanjing University, Nanjing 210046, China

Email: wangsl@nju.edu.cn

Tel: +86-25-83686016

Author: Mark Naylor

Email: Mark.Naylor@ed.ac.uk

Author: Hugh Sinclair

Email: Hugh.Sinclair@ed.ac.uk

**Corresponding author: LiangShu Wang

Postal address: No. 163 Xianlin Avenue, Nanjing University, Nanjing 210046, China

Email: lswang@nju.edu.cn

Tel: +86-25-83686016

ABSTRACT

The Tarim Basin became a closed continental sedimentary basin in the Cenozoic due to uplift of the western Kunlun, Tian Shan and the Altyn Tagh ranges in the context of the Indian-Asia collision. A north-northeast trending seismic profile across the basin reveals that Cenozoic strata comprise a wedge of sediments in the southern and northern regions generated by flexural subsidence overlain by a more uniform

regional sediment drape. We obtain the subsidence profiles across the basin at ~26 Ma, ~13 Ma, ~5 Ma and the present day using backstripping based on the sedimentary architecture shown in the seismic profile. We use a numerical finite elastic plate to model these subsidence profiles. Our modelling indicates that the southern and northern flexural depressions started to interfere to form a single flexural bulge within the basin since late Paleogene times. The flexural bulge migrated ~52 km toward the western Kunlun range since ~26 Ma, reflecting a decrease in the ratio of loads of the western Kunlun range versus the Tian Shan. We separate the sediment drape from the flexural subsidence according to the preceding modelling results. Our separating demonstrates that the thickness of the drape increased from 230±30 m at ~26 Ma to 1910±200 m at present, occupying ~30 % of Cenozoic strata in the profile. The rise in the base level since the Paleogene is estimated as 356±80 m by correcting for sediment loading of the drape. We adopt a decreasing basin width to model the evolution of the flexural subsidence, suggesting significant uplifting of the western Kunlun range and the Tian Shan from ~26 Ma to ~13 Ma, relative stable elevations in these ranges from ~13 Ma to ~5 Ma, and their rapid uplifts since ~5 Ma.

Keywords: Tarim Basin, Flexure, Ponding, Tian Shan, Western Kunlun

1. Introduction

The India-Asia collision caused large-scale intracontinental deformations (Molnar and Tapponnier, 1975; Tapponnier and Molnar, 1976; England and Houseman, 1986), and rejuvenated ancient orogens (Avouac et al., 1993; Yin et al., 1998; 2002; Yin, 2000; Yin and Harrison, 2000; Cowgill, 2010; Wang et al., 2013; Li et al., 2019). The Tarim Basin is bounded to the north by the Tian Shan, and to the southwest by the western Kunlun range and to the southeast by the Altyn Tagh range (Fig. 1). The basin became a closed continental sedimentary basin and was isolated from the

Paratethys Sea to the west due to the rejuvenations of these orogens (Graham et al., 1993; Jia et al., 1997; Sobel et al., 2003; Bosboom et al., 2011; 2014a; 2014b). Basinward thrusting of the Tian Shan and western Kunlun range also caused subsidence in the southern and northern flexural depressions of the Tarim Basin (Yang and Liu, 2002). Presently, it is an internally draining basin with a regional slope dip of 0.0005 to the north such that rivers sourced in the western Kunlun Shan drain across the basin to the northern side (Fig. 1). This configuration was typical since the Paleogene which implies that the south is a source of sediment to the whole basin (Sobel et al., 2003; Wei et al., 2013; Rittner et al., 2016). The flexural profiles across the basin reveal that Cenozoic strata comprise a wedge of sediments in the southern and northern regions generated by flexural subsidence overlain by a more uniform regional sediment drape (Jia et al., 1997; Yu et al., 2014; Li et al., 2015). Despite the wealth of publications regarding the Cenozoic subsidence history of the Tarim Basin (e.g., Cao et al., 1994; Yang and Liu, 2002; Yan et al., 2003), the evolution of the sediment ponding in the basin is not well constrained. The flexural profile appears to be nearly smooth with a single flexural bulge within the basin. This implies that the northern and southern flexural depressions are not independent and depend upon the relative loading of the northern and southern margins. If they were independent, there would be two separate forebulges. When the southern and northern flexural depressions of the Cenozoic Tarim Basin started to interfere is an open question. This requires an alternative modelling approach than the standard analytic solutions for flexural foreland basins (e.g., Flemings and Jordan, 1989; Watts, 2001) to explore the evolution of the Cenozoic Tarim Basin by flexural subsidence and sediment ponding. We applied an elastic finite plate model with a tectonic load on either side to model the subsidence history in the basin. We will refer to this model as

77 a finite plate model (Fig. 2) (as opposed to the semi-infinite or infinite plate models
78 that are generally used (e.g., Turcotte and Schubert, 2002)). Consequently, there will
79 be implications for subsidence and regional tectonics.

80 The Tarim Basin is significantly draped, reflecting the internally drained systems
81 of the basin (Fig. 1; Sobel et al., 2003). Standard models of the foreland basin do not
82 take into account a regional drape (e.g., Flemings and Jordan, 1989; Sinclair et al.,
83 1991; Sinclair, 2012). As a result, this is a process that is generally overlooked when
84 dissecting subsidence profiles (e.g., Sinclair et al., 1991; Yang and Liu, 2002; Liu and
85 Nummdal, 2004; Saura et al., 2015). The Tarim lithosphere underthrusts beneath the
86 western Kunlun range and the Tian Shan since the late Paleogene (Gao et al., 2000;
87 2013; Khao et al., 2001; Zhao et al., 2003; Li et al., 2019), which caused a decrease in
88 the width of the Tarim Basin (Fig. 2). It is also still an open question to determine
89 how the decreasing basin width affected the subsidence history in the Tarim Basin
90 (Cao et al., 1994; Yang and Liu, 2002; Yan et al., 2003). We explored the
91 consequences of the regional sediment drape and the decrease of the basin width
92 using the finite plate model.

93 We modelled the basement subsidence history using a two-dimensional (2-D)
94 finite elastic plate model based on the sedimentary architecture shown in the
95 north-northeast trending seismic profile (Fig. 2) across the basin. Our modelling
96 indicates that the lithospheric flexures on the southern and northern sides of the basin
97 have interfered with each other since late Paleogene times to form a single flexural
98 bulge within the basin. The migration of the flexural bulge records the evolution of
99 the relative loading on the southern and northern margins. In addition to the
100 subsidence in the southern and northern flexural depressions, there is a significant
101 component of base-level rise and draping of the basin caused by tectonic ponding and

internal drainage. We separated the sediment drape from the flexural subsidence, and its effects on the subsidence history in the basin were analyzed. We modelled the evolution of flexural subsidence with fixed and decreasing basin widths and discussed its implications on the growth of the western Kunlun range and the Tian Shan.

2. Geological background

The Tarim Basin is flanked on the north by the Tian Shan, on the southwest by the western Kunlun range (Fig. 1). The western Kunlun range is a Paleozoic accretionary orogenic belt between the Tarim Basin and the Qiangtang terrain (Matte et al., 1996; Yin and Harrison, 2000; Xiao et al., 2002). The Tian Shan originated from the accretions of several island arcs and the collisions of continental blocks in the Paleozoic (Windley et al., 1990; Wang et al., 2007; Charvet et al., 2011). The late Cenozoic rejuvenation of these two orogens caused the subsidence of the northern and southern depressions of the basin. Cenozoic strata in the southern depression comprise the Kashi Group (subdivided into the Aertashi, Qimugen, Kalataer, Wulagen and Bashibulak Formations from the bottom up), the Wuqia Group (subdivided into the Keziluoyi, Anjuan and Pakabulak Formations in an ascending order), the Artux Formation and the Xiyu Formation in an ascending order (Fig. 3) (Xinjiang BGMR, 1993; Zhang et al., 2004). The Cenozoic sedimentary sequences in northern depression consist of the Kumugeliemu, Suweiyi, Jidike, Kangcun, Kuqa and Xiyu formations in an ascending order (Fig. 3) (Zhang et al., 2004). We divided the Cenozoic strata into four units using four continuous seismic reflectors named T8, T6, T5 and T3. The T8, T6, T5 and T3 represent the bottom of the Kumugeliemu and Kashi groups, the bottom of the Jidike Formation and the upper part of the Kuziluoyi Formation, the bottom of the Kangcun and the Pakabulak Formations and the bottom of the Kuqa and Artux Formations, respectively (Fig. 3). Li et al. 2018 correlated the

127 seismic reflectors with the magnetostratigraphic studies (Huang et al., 2006; Charreau
128 et al., 2009; Zhang et al., 2014) in the foreland area of the southern Tian Shan, and
129 timed the ages of T8, T6, T5 and T3 as ~66 Ma, ~26 Ma, ~13 Ma and ~5.3 Ma,
130 respectively, assuming the four seismic reflectors are isochronous.

131 Sedimentological studies indicate the seaway connection between the Tarim and
132 the Tajik basins during the Cretaceous and the Paleogene (Bosboom et al., 2011;
133 2014a; 2014b), implying that the base levels in these two basins were the same during
134 the period (Fig. 1). The ponding of the Tarim Basin caused the regional sediment
135 drape and the rise in the base level (Bosboom et al., 2011; Carrapa et al., 2015; Yang
136 et al., 2015). However, the current base level in the Tarim Basin is ~530 m higher
137 than the Tajik Basin (Fig. 1c).

138 **3. Data**

139 The basic data for the subsidence modelling in the Tarim Basin was derived from
140 a ~610 km-long and 6-second-deep seismic profile (Fig. 4a) extending from the
141 western Kunlun fold-thrust belt in the south to the Kuqa fold-thrust belt in the north
142 (Fig. 1b). We converted the seismic time profile into a depth profile based on well
143 logging data near this profile and the interpretations of the seismic profiles in the
144 southern depression from Jiang et al. (2013). This seismic profile is oblique to these
145 two fold-thrust belts, thus it does not represent the width of the basin. Admittedly, the
146 width of the basin is one of the key parameters in our modelling (Fig. 1b). Hence, we
147 projected the profile onto a straight line transverse to the basin axis (purple dashed
148 line in Fig. 1b) so that it can be used in our 2-D finite plate model. The projected
149 straight profile is perpendicular to the western Kunlun range and oblique to the Tian
150 Shan (Fig. 1b). The Cenozoic strata in the projected profile are divided into four
151 layers by T8, T6, T5 and T3 (Fig. 4b).

We obtained the profiles of basement subsidence at ~26 Ma, ~13 Ma, ~5 Ma and to the present-day by backstripping Cenozoic strata in the projected profile. Decompaction parameters used in the calculation are derived from Sclater and Christie (1980) (Table 1); the lithology, the density, the top and bottom depths of each layer are obtained from the projected profile and well logging data. The epicontinental sea only reached the western margin of the basin in the Paleogene and became eventually isolated from the basin in the late Eocene (Bosboom et al., 2011; 2014a; Fig. 1), thus we ignored the eustatic sea-level changes. The paleobathymetry is estimated based on the sedimentary environment analyses of each stratigraphic unit (Guo et al., 2002; Li et al. 2004; 2005; Shao et al., 2006), and incorporates broad error bars.

Effects of various factors on the lithospheric rigidity, such as thermal structures, lithospheric composition, and mechanical weakening because of densely developed basement faulting, may be lumped into the effective elastic thickness of the lithosphere (Te) (Burov and Diament, 1995; Yang and Liu, 2002). Accordingly, the elastic constants of the lithosphere in the finite plate model are represented implicitly by its Te values. Standard values (Aitken, 2011) were used for Young's modulus E (5×10^{10} Pa), Poisson's ratio ν (0.25), crust density ρ_c (2700 kg m^{-3}), mantle density ρ_m (3300 kg m^{-3}) and gravitational acceleration g (9.81 m s^{-2}) in our model.

4. The finite plate model

4.1. The numerical model

We apply a 2-D finite elastic plate model to the subsidence modelling in the Cenozoic Tarim Basin. The elastic rheology has been applied to a large number of flexural basins (Turcotte, 1979; Burov and Diament, 1992), such as the central Alps

(Sinclair et al., 1991), the Sevier thrust belt (Liu and Nummdal, 2004), the Bolivian Andes (Prezzi et al., 2009), the NW Zagros (Saura et al., 2015) and the Tarim Basin (Yang and Liu, 2002). The cases indicate the 2-D elastic plate model can approximate the observed basement subsidence profiles in first-order.

Tectonic load and sediment load are imposed onto a finite elastic plate in the model. We call the tectonic load upon the horizontal datum as the topographic load. The topographic loads are reduced to two single line end loads with a width of 2 km imposed on the southern and northern boundaries of the plate (Fig. 5). Our model ignored the distribution of the thrust wedge topographic load due to lacking constrains for the rate of propagation of the thrust wedges of the western Kunlun range and the Tian Shan since the Paleogene. The major limitation of the end load is that it cannot simulate onlap of foreland sequence driven by changing the distribution of topography (Naylor and Sinclair, 2008), which do not affect the subsidence modelling.

To model the effect of the sediment load on the subsidence of the basement, we assume that the basin is filled to the horizontal datum (the top surface of the plate before deflection) by the sedimentary material with a density of 2683 kg/m^3 based on the average density of Cenozoic rocks from drilling data (Jia et al., 1997; Yang and Liu, 2002). We use the finite difference solution for the flexure equation based on a Python script called 'Gflex' (Wickert, 2016).

The main parameters in the finite plate model contain the length of the elastic plate W (representing the width of the basin), Te, E, ν, , L_S and L_N (topographic loads imposing on the southern and northern end of the plate), ρ_c, ρ_m, density of the sedimentary material ρ_s and g.

The Te, L_S and L_N are treated as variables in our modelling the subsidence history in the Tarim Basin. The optimal values for these three parameters are determined by minimizing the misfit between the observed and modelled subsidence profiles. There are certain trade-offs between the Te, L_S and L_N. We applied the downhill simplex algorithm (Wright et al., 1996) to find the best combination of these three variables. We utilize Python's scipy fmin function to implement the downhill simplex algorithm. We model the best combination of these three variables using the trial-error method carrying out through a Python program based on the 'Gflex' and the 'fmin.'

4.2. Model test

4.2.1. Effects of asymmetric loading

We explore the effect of the load of the mountain belts on either side on the flexural profile of the finite plate (Fig. 5). Assuming the Te value of 80 km, the wavelength of the deflection of the elastic plate is calculated as ~881 km by the following equation (Turcotte and Schubert, 2002):

$$\lambda_0 = 2\pi\left(\frac{ETe^3}{12(1-\nu)(\rho_m-\rho_s)g}\right)^{1/4} \quad (1)$$

The first scenario of the model sets the basin width (W) as 2500 km, which is over twice the value of λ_0. We apply identical topographic loads on both ends of the long elastic plate ($L_S = L_N$) (Fig. 5a). Two separate flexural bulges and a flat region with a considerable distance between them is generated; the northern and southern deflections of the plate are symmetrical. The profiles are independent of the distant load and each could be modelled separately as a semi-infinite plate. In the second scenario, W is taken as 1200 km (which is less than twice λ_0 but still greater than λ_0), as well L_S and L_N are unchanged (Fig. 5b). The southern and northern

225 deflections of the elastic plate interfere; nevertheless, two separate flexural bulges are
226 still present.

227 The third scenario sets W to 600 km which is less than λ_0, as well as symmetric
228 *Ls* & *Ln* (Fig. 5c). The model indicates that the northern and southern deflections of
229 the elastic plate are not independent, and only one single flexural bulge is present in
230 the middle of the plate (Fig. 5c). We repeat the analysis but with a lighter load
231 imposed upon the northern margin of the elastic plate ($L_N < L_S$) in the fourth scenario
232 (Fig. 5d). A deeper depression forms on the south side than on the north side; and yet
233 the flexural bulge shifts towards the lighter load on the northern side. The
234 consequence reveals that the migration of the central flexural bulge can reflect the
235 relative topographic load on both sides of the basin under the case that W is less than
236 λ_0. This configuration is closer to the profile across the modern Tarim Basin.

237 **4.2.2. Effects of sediment drape on subsidence of the basin**

238 We also explore the effects of the sediment drape on the finite plate. Applying a
239 uniform drape across the basin with constant flexural rigidity causes the whole basin
240 to depress uniformly (Fig. 5e). This result suggests that the shift in the position of the
241 flexural bulge with time is related to only the relative changes in load at both margins
242 of the basin; the shift is insensitive to the effects of the long wavelength regional
243 drape. Consequently, we can consider the evolutions of the sediment drape and the
244 flexural subsidence, separately.

245 **4.2.3. Effects of Te and basin width on deflection**

246 Since elastic flexure is a linear process (Turcotte and Schubert, 2002), we may
247 separately test the parameters determining the flexural deformation of the finite elastic
248 plate (Te and W). We construct two sets of experiments to test how the changing of

249 Te and W affects the flexural deformation of the finite plate. For each set of
250 experiments that investigate the role of one parameter, the other parameter is fixed.

251 In the first set of experiments, W is fixed at 600 km, and Te gradually increased
252 from 70 km to 130 km. The ratio of $W_{S,B}$ (the distance from the southern boundary
253 of the basin to the crest of the bulge) and W is more sensitive to changes in the
254 L_S/L_N under high Te value (Fig. 6a). Z_S and Z_N are the maximum subsidence in
255 the south and north sides of the basin, respectively. Z_S/Z_N increased with L_S/L_N
256 getting higher in the case that Te increases from 70 km to 130 km (Fig. 6b). Hence,
257 the migration of the flexural bulge and Z_S/Z_N in a rigid lithosphere can distinctly
258 reflect changes in the relative topographic load on either side.

259 In the second set of experiments, Te is fixed at 80 km, and W gradually
260 decreases from 700 km to 400 km. $W_{S,B}/W$ are more sensitive to changes in L_S/L_N
261 in the case that the basin width is small (Fig. 6c). Z_S/Z_N is also more sensitive to
262 changes in L_S/L_N under small W value (Fig. 6d). Consequently, the sensitivity of
263 the flexural bulge's migration and Z_S/Z_N to the relative topographic loads increases
264 with the decrease of W.

265 **5. Modelling the subsidence history in the internally drained system**

266 **5.1. Calculation of the sediment drape**

267 The growth of mountain topography induces the lithospheric flexural deformation
268 to form a flexural depression in the foreland region in the classic foreland basin model
269 (Allen and Allen, 2013). Sediments from the mountain range fill the depression to a
270 base level (such as sea level). This model needs to be adapted to the model of the
271 internally drained system. The assumption that a basin will fill to a fixed base level is
272 not suitable in the case that the basin is internally drained, ponding all available
273 sediment as a regional drape. Before modelling the evolution of flexural subsidence

coupled with the growth of mountain topography, we need to develop a correction that can estimate the evolution of the sediment drape with time and then separate it from the subsidence in the flexural depressions.

The flexural bulge has no sediments (in an underfilled basin) or the thinnest sediment (in an overfilled basin). We assumed that the uncompacted thickness of the sediments over the historical bulge is that of the drape sediments (Fig. 2). We subtracted the thickness of the drape of each layer from the corresponding layer; the remainder is the flexural subsidence caused by lithospheric flexure. Although these estimates, calculated from a 2-D seismic line across a large basin, have significant uncertainty, the first-order signal is identifiable with error bars accounting for the uncertainty. Given that the gradient of the present surface of the Tarim Basin is 0.0005, this can produce a ~10% correction to the drape thickness in basin margin at a distance of ~250 km from the bulge.

Additionally, several reverse faults tilted the Cenozoic strata in the basin, changing the shape of the middle part of the flexural profile (Figs. 4 and 5) (Lin et al., 2015; Li et al., 2016). We obtained a smooth flexural profile best fitting with the observed subsidence profile by using the finite plate model, ignoring the distortion caused by these reverse faults. Subsequently, we identified the positions of the historic flexural bulges of each layer in the best-fitting profile. We determined positions of the flexural bulge at ~26 Ma, ~13 Ma, ~5 Ma and the present, respectively.

The sedimental accommodation due to ponding, the space for the sediment drape, comprises the subsidence due to sediments load of the drape and the increased accommodation due to the rise in base level (Fig. 2). The former is the isostatic

298 respond to the drape. We can obtain the increased accommodation due to a rise in the
299 base level by subtracting the former from the thickness of the drape.

300 **5.2. Modelling the flexural subsidence**

301 We eliminated the effects of the drape to obtain the flexural subsidence by
302 subtracting the sediment drape from the basement subsidence (Fig. 2).

303 We modelled the evolution of the flexural subsidence in the basin using the finite
304 plate model, in order to analyze the evolution of flexural subsidence coupled with the
305 growth of the mountain topography. We modelled the evolution of the flexural
306 subsidence for fixed and decreasing W to explore the effects of the reduction in the
307 basin width due to underthrusting on the flexural subsidence profile across the basin.
308 The reduction in W over the four time intervals is equal to the sum of the cumulative
309 underthrusting beneath the western Kunlun range and the Tian Shan (Fig. 2; Table. 2).
310 The sums in four stages were derived from the forelandward onlap rate of the
311 basin-scale filling sequences (Homewood et al., 1986; Sinclair and Allen, 1992;
312 DeCelles and DeCelles, 2001; Naylor and Sinclair, 2008). The onlap rates were
313 constrained by a fine analysis of the sedimentary architecture revealed by the seismic
314 profiles crossing the foreland areas of the western Kunlun range and the Tian Shan,
315 about 300 km west of our profile (Li et al., 2019). The analysis indicated the historic
316 widths of the Tarim Basin at ~26 Ma, ~13 Ma, and ~5 Ma are 802 km, 719 km, and
317 569 km, respectively (Table. 2). The horizontal shortening rates across the western
318 Kunlun range could vary along its strike (Wang et al., 2001; Zheng et al., 2017),
319 suggesting that the underthrusting rates of the Tarim lithosphere could be different
320 along its strike. Furthermore, the projected profile is oblique to the Tian Shan. Thus,
321 the adopted values of the basin width could incorporate broad bias errors.

322 The evolutions of L_S and L_N shed new lights on the mountain building in the
323 western Kunlun range and the Tian Shan.

324 **6. Results**

325 **6.1 The sediment drape**

326 We obtained the basement subsidence profiles at ~26 Ma, ~13 Ma, ~5 Ma and the
327 present, respectively, by backstripping the Cenozoic strata (Figs. 7a-d). Figure 7
328 shows the modelling results of the subsidence profiles in the same reference system.

329 The best fitting results of these subsidence profiles (Figs. 7a-d) show a single
330 flexural bulge within the basin since the Paleogene. The flexural bulge occurred in the
331 site of 452 km in Figure 7 at ~26 Ma (Fig. 7a); it migrated to the site of 431 km at ~13
332 Ma (Fig. 7b), to the site of 419 km at ~5 Ma (Fig. 7c) and to the site of 400 km at
333 present (Fig. 7d). The flexural bulge migrated a total of ~52 km southwards in Figure
334 7 since ~26 Ma. We calculated the thickness of the sediment drape regardless of the
335 surface slope. The thickness of the sediment drape increased from 230±30 m to
336 1910±200 m from ~26 Ma to the present (Table. 3). About ~90% of the drape was
337 deposited after ~26 Ma. The flexural subsidence appeared only in the south side of the
338 profile at ~26 Ma, and occurred on either side after at least ~13 Ma. It reaches the
339 maximum of 5 km in the southern end of the basin. The sediment drape occupies ~30%
340 of the Cenozoic sediments in the profile. The thickness of the increased
341 accommodation due to the rise in the base level is estimated as 356±80 m by
342 correcting for sediment loading of the drape. It means that the base level in the Tarim
343 Basin rose 356±80 m in the Cenozoic (Table 3). The base level rose 40±15 m from
344 ~65 Ma to ~26 Ma, 70±20 m during ~26 Ma to ~13 Ma, 90±20 m during ~13 Ma to
345 ~5 Ma, and 150±25 m from ~5 Ma to the present (Table 3). The results show that the

optimal value of Te gradually increases from 86 km to 98 km from ~26 Ma to the present.

The modelled load on the southern basin margin required to approximate the basin increased progressively from 0.59 $\times 10^9$ Pa to 5.07 $\times 10^9$ Pa from ~26 Ma to the present, and for the modelled load on the northern margin from 0.37 $\times 10^9$ Pa to 4.45 $\times 10^9$ Pa (Figs. 7a–d). This implies significant increased topography of the western Kunlun range and the Tian Shan during this interval.

6.2. The flexural subsidence

We modelled the evolution of flexural subsidence using the finite plate model with the fixed and decreasing W.

The flexural subsidence modelling indicates that the modelled load of the western Kunlun range required to generate the basin subsidence gradually increased from 0.22 $\times 10^9$ Pa to 1.97 $\times 10^9$ Pa since ~26 Ma to the present under the fixed current basin width of 521 km, and for the load of the Tian Shan from 0.002 $\times 10^9$ Pa to 1.33 $\times 10^9$ Pa (Figs. 7e-h; Table 4). They are only half of the topographic loads derived from the basement subsidence modelling, suggesting a possible overestimate in the former modelling. The ratio of topographic loads between the western Kunlun range and the Tian Shan (L_S/L_N) decreased from 110 to 1.48 from ~26 Ma to present. It is compatible with the southward migration of the flexural bulge. The optimal value of Te increased from 38 km to 53 km from ~26 Ma to present. It is also only half of the Te values derived from the basement subsidence modelling (Figs. 7e-h). The model fit to the data improve (Fig. 7), but the main error is possibly explained by the distortion of the middle part of the flexural profile caused by the reverse faults.

The flexural subsidence modelling also suggests that the topographic load of the Tian Shan increased from 0.004 $\times 10^9$ Pa to 0.68 $\times 10^9$ Pa from ~26 Ma to ~13 Ma,

371 reaching half of its present load (1.33 $\times 10^9$ Pa) under the basin width decreasing from
372 802 km at ~26 Ma to 521 km at ~13 Ma (Figs. 7i–l; Table 2). The topographic load of
373 the western Kunlun range increased from 0.75 $\times 10^9$ Pa at ~26 Ma to 1.64 $\times 10^9$ Pa at
374 ~13 Ma, nearly four-fifths of its current topographic load (1.97 $\times 10^9$ Pa) (Table 4).
375 These indicate that both the ranges had increased significantly in elevation and
376 exceeded half of their current elevations at ~13 Ma. The topographic load of the
377 western Kunlun range increased slightly to 1.69 $\times 10^9$ Pa, and the load of the Tian
378 Shan decreased a little to 0.56 $\times 10^9$ Pa from ~13 Ma to ~5 Ma. The elevations of
379 these two ranges remained relatively steady. The topographic load of the Tian Shan
380 increased rapidly to 1.33 $\times 10^9$ Pa from ~5 Ma to the present; that of the western
381 Kunlun range also expanded to 1.97 $\times 10^9$ Pa (Figs. 7i–l). This scenario is different
382 from the progressive growth of these ranges revealed by the modelling with fixed W.
383 The ratio of the topographic loads (L_S/L_N) decreased from 186 to 1.48 since ~26 Ma.
384 The flexural subsidence modelling demonstrates that the optimal value of Te was 75
385 km at ~26 Ma and reduced to 55 km at ~13 Ma; then it declined to 46 km at ~5 Ma,
386 and rather increased to 53 km at present (Figs. 7i–l). Given the broad bias errors in
387 backstripping and the adopted values of the basin width, there is uncertainty in the
388 estimate of optimal value of Te.

389 **6.3. The modelled subsidence history**

390 We recovered the evolution of the basement subsidence and the depositional base
391 level in the Tarim Basin with the decreasing width due to the Tarim lithosphere's
392 underthrusting since ~26 Ma (Fig. 8) through forward. There was one flexural
393 depression in the southern part of the profile at ~26 Ma. In contrast, no detectable
394 flexure occurs in the northern part of the profile (Fig. 8a), reflecting a delay of
395 mountain building in the Tian Shan relative to the western Kunlun range. Two

flexural depressions occurred in both sides of the profile from ~26 Ma to ~13 Ma. The basement subsidence increased by ~2 km in the northern depression during this stage and by ~3 km in the southern depression (Fig. 8b), suggesting significant uplifts of these two ranges. The basement subsidence in the middle part of the profile increased by ~0.5 km from ~13 Ma to ~5 Ma, and continued to increase rapidly by ~0.8 km from ~5 Ma to the present. Furthermore, the base level in the basin has risen rapidly by 240±20 m since ~13 Ma, causing an increase of ~1.3 km in the thickness of the sediment drape (Table 3). The subsidence due to the sediment load of the drape caused the acceleration of subsidence in the middle part of the basin. The basement subsidence increased by ~1 km in the southern and northern depressions from ~13 Ma to ~5 Ma. It continued to increase by ~1.5 km in the southern depression and by ~2 km in the northern depression since ~5 Ma. The basement subsidence reaches the maximum amount of ~6.5 km in the southern boundary of the profile (Figs. 8c & 8d).

7. Discussion

We applied the finite plate model to reconstruct the evolution of the flexural subsidence, the sediment drape in the basin and the topographic growth on basin margins according to the seismic profile across the Tarim Basin. Here we analyze the effects of the model parameters and its implications on the Cenozoic evolution of the basin and the mountain buildings in the western Kunlun range and the Tian Shan.

7.1. The optimal Te value

Te is one of key parameters for modelling lithospheric flexural deflection. In our model, the optimal Te values were determined by minimizing the misfit between the observed and predicted subsidence profiles. Modelling the optimal values of Te is affected by the sediment drape and the basin width W (Fig. 7). The optimal value of Te for the lithosphere of the modern Tarim is 98 km derived from the basement

421 subsidence profiles. However, the modelling based on the flexural subsidence profiles
422 generated a Te value of 53 km at present. The Te value of 53 km is closer to the
423 median value between 66 ± 7 km estimated from the lithospheric thermo-rheological
424 structure (Liu et al., 2006) and 45 km from the averaging gravity-derived estimates
425 (Jiang et al., 2004). Consequently, we probably overestimated the Te value because
426 of neglecting the effect of the sediment drape in the basement subsidence modelling.
427 The predicted optimal values of Te increased from 38 km to 53 km since ~26 Ma
428 in case that the value of W keeps constant. Many factors that affect lithospheric
429 rheology (e.g., geothermal condition, lithospheric composition, and mechanical
430 weakening) may be expressed through the Te (Burov and Diament, 1995). The
431 mechanical weakening due to rifting could cause a decrease in Te, but could not cause
432 an increase in it. There has been no magmatic activity in the Tarim Basin since the
433 late Paleozoic (Yang et al. 2007), so the Tarim's lithosphere underwent little
434 compositional change in the lithospheric composition during the Cenozoic. The
435 effects of changes in the composition on Te of the Tarim Basin is negligible and has
436 not considered here. The last major tectono-thermal event in the Tarim Basin was the
437 Early Permian basaltic eruption, which occurred at ca. 277 Ma (Yang et al. 2007), and
438 paleogeothermal gradients in this area decreased slowly from 2.7–2.2 ℃/100 m during
439 the Paleogene to ~2.1 ℃/100 m at present (Wang et al., 1995; Liu et al., 2006; Chang
440 et al., 2017). The reason for the increasing Te value of the Tarim's lithosphere is not
441 clear, but the results are consistent with the cooling process in the Tarim Basin (Wang
442 et al., 1995; Yang and Liu, 2002). Geothermal studies indicate an average heat flow of
443 ~44 mW m^{-2} in the modern Tarim Basin (Hu et al., 2000; Liu et al., 2015). The Te
444 values are sensitive to changes in the heat flow in the case that the average heat flow
445 ranges from 40 mW m^{-2} to 70 mW m^{-2} (Hyndman et al., 2009; He et al., 2017).

446 Hence, the cooling process in the Tarim Basin may have played a more important role
447 in the increase of the Te value than the mechanical weakening and the lithospheric
448 composition.

449 Moreover, the modelled optimal value of Te decreased from ~26 Ma to ~5 Ma,
450 and the value at ~26 Ma and ~13 Ma is even higher than the modern Te value in
451 cases that the value of W decreases. The decrease of Te is contrary to the cooling
452 process in the Tarim Basin (Liu et al., 2006; Chang et al., 2017). These two
453 predictions indicate that a larger W value leads to a larger predicted optimal value of
454 Te. Consequently, the main factor potentially responsible for the abnormally high Te
455 value is possible our overestimating the value of W since ~26 Ma. Its decreases are
456 equal to the cumulative underthrusting of the Tarim lithosphere (Fig. 2; Table 2). The
457 underthrusting values were estimated from the forelandward onlaps identified from
458 the seismic profile (Li et al., 2019), about 300 km west of our profile. GPS
459 measurements show that the horizontal shortening rates across the western Kunlun
460 range vary along its strike (Wang et al., 2001; Zheng et al., 2017), suggesting that the
461 underthrusting rates of Tarim lithosphere could be different along its strike. Thus, the
462 adopted values were probably too big, producing abnormally high values of Te from
463 ~26 Ma to ~5 Ma. Nonetheless, if the reduction in the basin width due to the
464 underthrusting (Khao et al., 2001; Zhao et al., 2003; Gao et al., 2013) is completely
465 overlooked, the Te values for the ancient Tarim lithosphere must be underestimated.

466 Over the long term subsidence history of the Tarim basin, viscous flow and stress
467 relaxation may be expected, which are not included in the purely elastic model. We
468 expect the visco-elastic model would smooth the rate at which the slab profiles
469 respond, particularly to changes in the relative load between the two ranges (Turcotte
470 and Schubert, 2002). However, we do not have sufficient temporal resolution to tease

out the effects of plastic or viscous deformation based on the seismic profile. Therefore, the finite elastic plate model was used for modelling the subsidence profiles across the Tarim Basin.

7.2. Ponding of the Tarim Basin

The underthrusting of the Tarim lithosphere beneath the western Kunlun range and the Tian Shan may progressively narrow the corridor between them during late Cenozoic times (Yin et al., 2002; Sobel et al., 2003; Wei et al., 2013; Bosboom et al., 2014a; 2014b; Yang et al., 2015), until a barrier caused the basin to become internally drained. The closure caused the sediments sourced from the ranges surrounding the Tarim Basin to be trapped to form the regional sediment drape; this was decoupled from the topographic growth in the ranges. The large internally drained area persists till now due to that uplift of surrounding ranges overwhelms the fluvial system and defeats the channel network in the arid region with low precipitation (Sobel et al., 2003). The thickness of the sediment drape increased from 230±30 m to 1910±200 m since ~26 Ma, occupying ~30% of Cenozoic strata in the profile, suggesting the same volume of the late Cenozoic in the basin formed due to ponding and the rest due to flexure. About eighty-nine percent of the sediment drape occurred after ~26 Ma (Table 3; Figs. 7a–d).

We estimated a rise of 356±80 m in the base level of the Tarim Basin in the Cenozoic, based on the thickness of the sediment drape (Fig. 7). The base level in the modern Tarim Basin is ~530 m higher than that of the Tajik Basin, almost the same in the Paleogene (Bosboom et al., 2011). The estimated rise in the base level is smaller than the difference between the current base levels of these two basins. This suggests that the proportion of the sediment drape to the total Cenozoic sediments in the basin could be even larger than our estimation (~30%). Yu et al. (2015) predicted that the

topography in the Tarim Basin uplifted 800 m during the Cenozoic relying on Airy local isostasy. It is significantly larger than our estimate and even the difference between the base levels in the Tarim and Tajik Basins (Fig. 1). This reveals that neglecting the deflection of the Tarim lithosphere may cause an overestimate of the basal level rise.

7.3. The growth of asymmetric topography on the basin margins

The uplifts of the western Kunlun range and the Tian Shan following the Indo-Asian collision caused flexural subsidence in the southern and northern margins of the Tarim basin (Lu et al., 1994; Yin et al., 1998; 2002; Yang and Liu, 2002). The asymmetric growth of these two ranges was recorded by the migration of the flexural bulge in the basin.

Our modelling reveals that the flexural subsidence generated by loading from the south and the north formed a common flexural bulge in the center of the basin since late Paleogene times. The flexural bulge migrated ~52 km southward from the site of 452 km at ~26 Ma to the site of 400 km at present (Fig. 7); this recorded a reduction in the ratio of the two loads of the western Kunlun range to the Tian Shan (L_S/L_N) since ~26 Ma. The southward migration of the flexural bulge could be influenced by two controlling factors: the ratio of loads of the western Kunlun range versus the Tian Shan; the contrast in the lithospheric underthrusting rates beneath the two ranges (Sinclair and Naylor, 2012). The predicted decreasing ratio of the southern and the northern loads is consistent with the southward migration of the bulge. However, the contrast in the lithospheric underthrusting rates is not clear due to lack of constrains for the underthrusting rates along the profile since ~26 Ma as described in Section 7.1. This inference is also compatible with GPS measurements that the current shortening

520 rate across the western Kunlun range of 3 ± 2 mm/yr (Wang et al., 2011) is less than
521 that across the middle Tian Shan of ~10 mm/yr (Zubovich et al., 2010).

522 **7.4. Implications of modelling under decreasing basin width for topographic**
523 **growth**

524 The Tarim Basin narrowed since late Paleogene times (Fig. 2), due to
525 underthrusting of the Tarim lithosphere beneath the western Kunlun range (Khao et
526 al., 2001; Gao et al., 2000) and the Tian Shan (Zhao et al., 2003; Gao et al., 2013; Li
527 et al., 2019). The mechanics of the subsidence process under the decreasing Tarim
528 Basin width is still debatable (e.g., Cao et al., 1994; Yang and Liu, 2002; Yan et al.,
529 2003).

530 Our modelling predicts that topographic loads of the western Kunlun range and
531 the Tian Shan increased significantly from ~26 Ma to ~13 Ma (Fig. 9) and that this
532 was associated with a decreasing basin width. Low-temperature thermochronology
533 studies indicate that exhumation of the western Kunlun range (Sobel and Dumitru,
534 1997) and the Tian Shan (Dumitru et al., 2001) initiated during late Oligocene times.
535 The southern Tian Shan foreland basin began to accommodate deposits at the end of
536 the Oligocene (Li et al., 2019). These previous ages are complemented by our results.
537 The predicted topographic loads of these two ranges kept relatively steady during ~13
538 Ma to ~5 Ma, and increased again since ~5 Ma (Fig. 9). Our prediction of the
539 increasing topographic load of the range since ~5 Ma is supported by the increase in
540 the sedimentation rate in the piedmont of the Tian Shan at ~6 Ma (Jing et al., 2011)
541 and ~4 Ma (Charreau et al., 2008). The increasing topographic load of the Tian Shan
542 at ~5 Ma could be responsible for the main deformation of the Kuqa fold-thrust belt
543 since the Pliocene (Chen et al., 2004).

8. Conclusions

We modelled the subsidence history in the internally drained Tarim Basin using the finite plate model based on the north-northeast trending seismic profile across the whole basin. Our modelling indicates that the southern and northern flexural depressions started to interfere to form a single flexural bulge within the basin since the late Paleogene. The combined flexural bulge migrated 52 km toward the western Kunlun range since ~26 Ma, reflecting a decrease in the ratio of loads of the western Kunlun range versus the Tian Shan. In addition to the flexural subsidence, there is a significant component of base-level rise and draping of the basin caused by tectonic ponding and internal drainage. The modelling results also demonstrates that the thickness of the drape increased from 230±30 m at ~26 Ma to 1910±200 m at present, occupying ~30 % of Cenozoic strata in the profile. The depositional base level of the basin rose 356±80 m since the Paleogene. The flexural subsidence only appeared in the south side of the basin before ~26 Ma, and occurred in both sides after this age. It reaches the maximum of 5 km in the southern margin. Our modelling indicates the western Kunlun range and the Tian Shan uplifted significantly from ~26 Ma to ~13 Ma, kept relative steady effective elevations during ~13 Ma to ~5 Ma, and uplifted since ~5 Ma under a decreasing basin width. The predicted increase in the optimal value of Te since ~26 Ma is consistent with the cooling history of the Tarim basin. Neglecting the effect of the sediment drape leads to overestimates of the calculation of Te and of the tectonic loads on the basin margins.

Acknowledgments

This work was supported by the National Natural Science Foundation of China [grant numbers 41372201, 41672198], the National Key R&D Plan of China [grant number 2017YFC0601402] and the National Science and Technology Major Project of China

569 [grant number 2017ZX05008001]. This study benefited from discussions with Prof.
570 Shaowen Liu and Dr. Gareth Johnson. Prof. Yuejun Li and an anonymous reviewer
571 are warmly thanked for reviews of the manuscript. We are also grateful for the help
572 by Dr. Jonathan Craig (the handling editor).

573 **References**

574 [1] Aitken, A. R., 2011. Did the growth of Tibetan topography control the locus and
575 evolution of Tien Shan mountain building?. Geology, 39, 459–462.
576 http://dx.doi.org/10.1130/G31712.1

577 [2] Allen, P. A., & Allen, J. R., 2013. Basin Analysis: Principles and Application to
578 Petroleum Play Assessment. Wiley-Blackwell Publishing, UK, pp. 326–339.

579 [3] Avouac, J. P., Tapponnier, P., Bai, M., You, H., & Wang, G., 1993. Active
580 thrusting and folding along the northern Tien Shan and late Cenozoic rotation of
581 the Tarim relative to Dzungaria and Kazakhstan. Journal of Geophysical
582 Research: Solid Earth, 98, 6755–6804. http://dx.doi.org/10.1029/92JB01963

583 [4] Bosboom, R. E., Dupont-Nivet, G., Houben, A. J. P., Brinkhuis, H., Villa, G.,
584 Mandic, O., Stoica, M., Zachariasse, W, J., Guo, Z, J., Li, C, X., & Krijgsman,
585 W., 2011. Late Eocene sea retreat from the Tarim Basin (west China) and
586 concomitant Asian paleoenvironmental change. Palaeogeography
587 Palaeoclimatology Palaeoecology, 299, 385-398.
588 http://dx.doi.org/10.1016/j.palaeo.2010.11.019

589 [5] Bosboom, R., Dupont-Nivet, G., Grothe, A., Brinkhuis, H., Villa, G., Mandic, O.,
590 Stoica, M., Huang, W., Yang, W., Guo, Z, J., & Krijgsman, W., 2014a. Linking
591 Tarim Basin sea retreat (west China) and Asian aridification in the late Eocene.
592 Basin Research, 26, 621–640. http://dx.doi.org/10.1111/bre.12054

[6] Bosboom, R., Dupont-Nivet, G., Grothe, A., Brinkhuis, H., Villa, G., Mandic, O., Stoica, M., Kouwenhoven, T., Huang, W, T., Yang, W., Guo, Z, J., 2014b. Timing, cause and impact of the late Eocene stepwise sea retreat from the Tarim Basin (west China). Palaeogeography Palaeoclimatology Palaeoecology, 403, 101–118. http://dx.doi.org/ 10.1016/j.palaeo.2014.03.035

[7] Burov, E. B., Diament, M., 1992. Flexure of the continental lithosphere with multilayered rheology. Geophysical Journal International, 109, 449–468. https://doi.org/10.1111/j.1365-246X.1992.tb00107.x

[8] Burov, E. B., and M. Diament., 1995. The effective elastic thickness (Te) of continental lithosphere: What does it really mean?. Journal of Geophysical Research, 100, 3905–3927. http://dx.doi.org/10.1029/94JB02770

[9] Cao, S., Chen, F., Luo, C., 1994. Numerical modelling of subsidence mechanism of a Meso-Cenozoic foreland basin in north Tarim. Oil & Gas Geology, 15, 113–120. (in Chinese with English abstract)

[10] Carrapa, B., Decelles, P. G., Wang, X., Clementz, M. T., Mancin, N., Stoica, M., Kraatz, B., Meng, J., & Abdulov, S., 2015. Tectono-climatic implications of Eocene paratethys regression in the Tajik basin of central Asia. Earth & Planetary Science Letters, 424, 168–178. http://dx.doi.org/10.1016/j.epsl.2015.05.034

[11] Chang, J., Qiu, N. S., & Xu, W., 2017. Thermal regime of the Tarim Basin, Northwest China: a review. International Geology Review, 59, 45-61. http://dx.doi.org/10.1080/00206814.2016.1210546

[12] Charreau, J., Avouac, J. P., Chen, Y., Stéphane Dominguez, & Gilder, S., 2008. Miocene to present kinematics of fault-bend folding across the Huerguosi anticline, northern Tianshan (China), derived from structural, seismic, and

617 magnetostratigraphic data. Geology, 36(11), 871-874.
618 http://dx.doi.org/10.1130/G25073A.1
619 [13] Charreau, J., Gumiaux, C., Avouac, J. P., Augier, R., Chen, Y., Barrier, L., Gilder,
620 S., Dominguez, S., Charles, N., & Wang, Q., 2009. The Neogene Xiyu Formation,
621 a diachronous prograding gravel wedge at front of the Tian Shan: Climatic and
622 tectonic implications. Earth and Planetary Science Letters, 287, 298–350.
623 http://dx.doi.org/10.1016/j.epsl.2009.07.035
624 [14] Charvet, J., Laurent-Charvet, S., Faure, M., Cluzel, D., Jong, K.D., 2011.
625 Paleozoic tectonic evolution of the Tianshan belt, NW China. Science China:
626 Earth Sciences, 2, 166–184. http://dx.doi.org/10.1007/s11430-010-4138-1
627 [15] Chen, S., Tang, L., Jin, Z., Jia, C., & Pi, X., 2004. Thrust and fold tectonics and
628 the role of evaporites in deformation in the western Kuqa foreland of Tarim Basin,
629 northwest China. Marine & Petroleum Geology, 21(8), 1027-1042.
630 http://dx.doi.org/10.1016/j.marpetgeo.2004.01.008
631 [16] Cowgill, E., 2010. Cenozoic right-slip faulting along the eastern margin of the
632 Pamir salient, northwestern China. Geological Society of America Bulletin, 122,
633 145–161. http://dx.doi.org/10.1130/B26520.1
634 [17] Decelles, P. G., & Decelles, P. C., 2001. Rates of shortening, propagation,
635 underthrusting, and flexural wave migration in continental orogenic systems.
636 Geology, 29, 135–138.
637 https://doi.org/10.1130/0091-7613(2001)029<0135:ROSPUA>2.0.CO;2
638 [18] Dumitru, T.A., Zhou, D., Chang, E.Z., Graham, S.A., Hendrix, M.S., Sobel, E.R.,
639 & Caroll, A.R., 2001. Uplift, exhumation, and deformation in the Chinese Tian
640 Shan. In: Hendrix, M.S., Davis, G.A. (Eds.), Paleozoic and Mesozoic tectonic
641 evolution of central Asia: From continental assembly to intracontinental

642 deformation. Geological Society of America Memoir, 194, 71–99.
643 http://dx.doi.org/10.1029/2003EO060011
644 [19] England, P., Houseman, G., 1986. Finite strain calculations of continental
645 deformation: Comparison with the India-Asia collision zone. Journal of
646 Geophysical Research, 91, 3664 –3676.
647 http://dx.doi.org/10.1029/JB091iB03p03664
648 [20] Flemings, P.B., and Jordan, T.E., 1989. A synthetic stratigraphic model of
649 foreland basin development. Journal of Geophysical Research: Solid Earth and
650 Planets, 94, 3851–3866. http://dx.doi.org/10.1029/JB094iB04p03851
651 [21] Gao, R., Huang, D. D., Lu, D. Y., Qian, G. H., Li, Y. K., Kuang, C. Y., Li, Q. S.,
652 Li, P. W., Feng, R. J., & Ye, G., 2000. Deep seismic reflection profile across the
653 juncture zone between the Tarim basin and the west Kunlun Mountains. Chinese
654 Science Bulletin, 24, 2281-2286. http://dx.doi.org/10.1007/BF02886369
655 [22] Gao, R., Hou, H, S., Cai, X, Y., Knapp, J. H., He, R, Z., Liu, J, K., Xiong, X, S.,
656 Guan, Y., Li, W, H., Zeng, L, S., & Roecker, S, W., 2013. Fine crustal structure
657 beneath the junction of the southwestern Tian Shan and Tarim Basin, NW China.
658 Lithosphere, 5, 382-392. http://dx.doi.org/10.1130/L248.1
659 [23] Graham, S. A., Hendrix, M. S., Wang, L. B., & Carroll, A. R., 1993. Collisional
660 successor basins of western China: impact of tectonic inheritance on sand
661 composition. Geological Society of America Bulletin, 105(3), 323-344.
662 https://doi.org/10.1130/0016-7606(1993)105<0323:CSBOWC>2.3.CO;2
663 [24] Guo, X. P., Ding, X. Z., He, X. X., Li, H. M., Su, X., & Peng, Y., 2002. New
664 progress in the study of marine transgressional events and marine strata of the
665 Meso-Cenozoic in the Tarim Basin. Acta Geologica Sinica-Chinese Edition, 76,
666 299–307(in Chinese with English Abstract).

667 [25] He, L.J., Xu, H. H., Liu, Q. Y., 2017. Tectono-thermal modeling of the foreland
668 basins: a case study of the Longmenshan foreland basin. Earth Science Frontier, 3,
669 127–136. (in Chinese with English abstract)
670 [26] Homewood, P., Allen, P.A. and Williams, G.D., 1986. Dynamics of the Molasse
671 Basin of western Switzerland. Foreland basins. pp.199-217.
672 [27] Hu, S.B., He, L.J. & Wang, J.Y., 2000. Heat flow in the continental area of China:
673 a new dataset. Earth and Planetary Science Letters, 2, 407–419.
674 https://doi.org/10.1016/S0012-821X(00)00126-6
675 [28] Huang, B. C., Piper, J. D. A., Peng, S. T., Liu, T., Li, Z., Wang, Q. C., & Zhu, R.
676 X., 2006. Magnetostratigraphic and rock magnetic constraints on the history of
677 Cenozoic uplift of the Chinese Tian Shan. Earth and Planetary Science Letters,
678 251, 346-364. http://dx.doi.org/10.1016/j.epsl.2006.09.020
679 [29] Hyndman, R. D., Currie, C. A., Mazzotti, S., Frederiksen, A., 2009. Temperature
680 control of continental lithosphere elastic thickness, Te vs Vs. Earth and Planetary
681 Science Letters, 3-4, 539–548. https://doi.org/10.1016/j.epsl.2008.11.023
682 [30] Jia, C.Z., Wei, G.Q., Wang, L.S., Jia, D., & Guo, Z.J., 1997. Tectonic
683 Characteristics and Petroleum, Tarim Basin, China. Petroleum Industry Press,
684 Beijing, pp. 1-295. (in Chinese)
685 [31] Jiang, X., Jin, Y., and McNutt, M.K., 2004. Lithospheric deformation beneath the
686 Altyn Tagh and West Kunlun faults from recent gravity surveys. Journal of
687 Geophysical Research: Solid Earth, 109, B05406.
688 http://dx.doi.org/10.1029/2003jb002444
689 [32] Jiang, X. D., Li, Z. X., Li, H. B., 2013. Uplift of the west Kunlun Shan, northern
690 Tibetan Plateau, dominated by; brittle thickening of the upper crust. Geology, 4,
691 439-442. https://doi.org/10.1130/G33890.1

692 [33] Jiang, X. D., 2014. Dynamic support of the Tien Shan lithosphere based on
693 flexural and rheological modelling. Journal of Asian Earth Sciences, 93, 37-48.
694 http://dx.doi.org/10.1016/j.jseaes.2014.07.006
695 [34] Jing, X. H., Shen, Z. Y., Wang, X., Yu, Y. L., & Pan, X. Q., 2011.
696 Magnetostratigraphic construct of Awate section in the north Tarim Basin: the
697 impulse uplift of Tian Shan. Chinese Journal of Geophysics, 54, 334–342.
698 http://dx.doi.org/10.1002/cjg2.1616
699 [35] Khao, H., Gao, R., Rau, R. J., Shi, D., Chen, R. Y., Guan, Y., & Wu, F, T., 2001.
700 Seismic image of the Tarim Basin and its collision with Tibet. Geology, 29, 575.
701 http://dx.doi.org/10.1130/0091-7613(2001)0292.0.CO;2
702 [36] Li, C., Wang, S, L., & Wang, L, S., 2019. Tectonostratigraphic history of the
703 Tian Shan, China: seismic profiling evidence, Journal of Asian Earth Sciences, 1,
704 101–114. https://doi.org/10.1016/j.jseaes.2018.08.017
705 [37] Li, S. J., Wang, Q.C., Li, Z., 2005. Characteristics of Mesozoic and Cenozoic
706 heavy minerals from Kuche River section in Kuche depression and their
707 geological implications. Acta Petrol Mineral, 24, 53–61. (in Chinese with English
708 abstract)
709 [38] Li, Y. J., Wen, L., Yang, H. J., Zhang, G. Y., Shi, J., Peng, G. X., Hu, J, F., Luo, J,
710 C., Huang, Z, B., Chen, Y, G., & Zhang, Q., 2015. New discovery and geological
711 significance of late Silurian–Carboniferous extensional structures in Tarim Basin.
712 Journal of Asian Earth Sciences, 98, 304–319.
713 http://dx.doi.org/10.1016/j.jseaes.2014.11.020
714 [39] Li, Y. J., Zhang, Q., Zhang, G. Y., Tian, Z. J., Peng, G. X., Qiu, B., Huang, Z, B.,
715 Luo, J, C., Wen, L., Zhao, Y., & Jia, T, G., 2016. Cenozoic faults and faulting
716 phases in the western Tarim Basin (NW China): effects of the collisions on the

717 southern margin of the Eurasian plate. Journal of Asian Earth Sciences, 132, 40–
718 57. http://dx.doi.org/10.1016/j.jseaes.2016.09.018
719 [40] Li, Z., Song, W.J., Peng, S.T., Wang, D.X., Zhang, Z.P., & Li, Z., 2004.
720 Mesozoic–Cenozoic tectonic relationships between the Kuqa subbasin and Tian
721 Shan, northwest China: constraints from depositional records. Sedimentary
722 Geology, 172, 223–249. http://dx.doi.org/10.1016/j.sedgeo.2004.09.002
723 [41] Liu, S. F., Nummedal, D., 2004. Late Cretaceous subsidence in Wyoming:
724 Quantifying the dynamic component. Geology, 5, 397–400.
725 https://doi.org/10.1130/G20318.1
726 [42] Liu, S. W., Wang, L. S., Li, C., Zhang, P., & Li, H., 2006. Lithospheric
727 thermo-rheological structure and Cenozoic thermal regime in the Tarim Basin,
728 Northwest China. Acta Geologica Sinica, 80, 344–350. (in Chinese with English
729 abstract)
730 [43] Liu, S. W., Lei, X., and Wang, L. S., 2015. New heat flow determination in
731 northern Tarim Craton, northwest China. Geophysical Journal international, 200,
732 1194–1204. https://doi.org/10.1093/gji/ggu458
733 [44] Lin, B., Zhang, X., Xu, X., Yuan, J., Yuan, N., & Zhu, J., 2015. Features and
734 effects of basement faults on deposition in the Tarim Basin. Earth-Science
735 Reviews, 145, 43–55. http://dx.doi.org/10.1016/j.earscirev.2015.02.008
736 [45] Lu, H. F., Howell, D. G., Jia, D., Cai, D. S, Wu, S. M., Chen, C. M., Shi, Y. S., &
737 Valin, Z. C., 1994. Rejuvenation of the Kuqa foreland basin, northern flank of the
738 Tarim basin, northwest China. International Geology Review, 36, 1151–1158.
739 http://dx.doi.org/10.1080/00206819409465509
740 [46] Matte, P., Tapponnier, P., Arnaud, N., Bourjot, L., Avouac, J. P., Vidal, Ph., Liu,
741 Q., Pan, Y., & Wang, Y., 1996. Tectonics of western Tibet, between the Tarim

742 and the Indus. Earth and Planetary Science Letters, 142, 311-330.
743 http://dx.doi.org/10.1016/0012-821X(96)00086-6
744 [47] Molnar, P., and Tapponnier, P., 1975. Cenozoic tectonics of Asia: effects of a
745 continental collision. Science, 189, 419–426.
746 http://dx.doi.org/10.1126/science.189.4201.419
747 [48] Naylor, M., & Sinclair, H. D., 2008. Pro-vs. Retro-foreland basins. Basin
748 Research, 20, 285–303. http://dx.doi.org/10.1111/j.1365-2117.2008.00366.x
749 [49] Prezzi, B. C., Uba, E. C., Götze, H., 2009. Flexural isostasy in the Bolivian
750 Andes: Chaco foreland basin development. Tectonophysics, 3-4, 526–543.
751 https://doi.org/10.1016/j.tecto.2009.04.037
752 [50] Rittner, M., Vermeesch, P., Carter, A., Bird, A., Stevens, T., Garzanti, E., Andò,
753 S., Vezzoli, G., Dutt, R., Xu, Z., and Lu, H., 2016, The provenance of
754 Taklamakan desert sand. Earth and Planetary Science Letters, 437, 127–137.
755 http://dx.doi.org/10.1016/j.epsl.2015.12.036
756 [51] Saura, E., Garcia-Castellanos, D., Casciello, E., Parravano, V., Urruela, A., &
757 Vergés, J., 2015. Modeling the flexural evolution of the Amiran and
758 Mesopotamian foreland basins of NW Zagros (Iran-Iraq). Tectonics, 3, 377-395.
759 https://doi.org/10.1002/2014tc003660
760 [52] Sclater, J. G., & Christie, P. A. F., 1980. Continental stretching: an explanation of
761 the Post-Mid-Cretaceous subsidence of the central North Sea Basin. Journal of
762 Geophysical Research: Solid Earth, 85, 3711-3739.
763 http://dx.doi.org/10.1029/JB085iB07p03711
764 [53] Shao, L. Y., He, Z. P., Gu, J. Y., Luo, W. L., Jia, J. H., Liu, Y. F., & Zhang, P.,
765 2006. Lithofacies paleogeography of the Paleogene in Tarim Basin. Journal of
766 Palaeogeography, 8, 353–364. (in Chinese with English Abstract)

767 [54] Sinclair, H.D., Coakley, B.J., Allen, P.A. and Watts, A.B., 1991. Simulation of
768 foreland basin stratigraphy using a diffusion model of mountain belt uplift and
769 erosion: an example from the central Alps, Switzerland. Tectonics, 3, 599-620.
770 http://dx.doi.org/10.1029/90TC02507
771 [55] Sinclair, H.D. and Allen, P.A., 1992. Vertical versus horizontal motions in the
772 Alpine orogenic wedge: stratigraphic response in the foreland basin. Basin
773 Research, 3-4, 215-232. http://dx.doi.org/10.1111/j.1365-2117.1992.tb00046.x
774 [56] Sinclair, H.D, 2012. Thrust wedge/foreland basin systems. Tectonics of
775 Sedimentary Basins: Recent Advances. Blackwell, Oxford, pp.522-537.
776 [57] Sinclair, H. D., Naylor, M., 2012. Foreland basin subsidence driven by
777 topographic growth versus plate subduction. Geological Society of America
778 Bulletin, 3, 368-379. http://dx.doi.org/10.1130/b30383.1
779 [58] Sobel, E. R., Dumitru, T. A., 1997. Thrusting and exhumation around the margins
780 of the western Tarim basin during the India-Asia collision. Journal of
781 Geophysical Research Solid Earth, B3, 5043-5063.
782 http://dx.doi.org/10.1029/96JB03267.
783 [59] Sobel, E. R., Hilley, G. E., & Strecker, M. R., 2003. Formation of internally
784 drained contractional basins by aridity-limited bedrock incision. Journal of
785 Geophysical Research: Solid Earth, B7, 2344.
786 https://doi.org/10.1029/2002JB001883
787 [60] Tapponnier, P., and Molnar, P., 1976. Slip-line field theory and large-scale
788 continental tectonics. Nature, 264, 319 – 324. http://dx.doi.org/10.1038/264319a0
789 [61] Turcotte, D. L., 1979. Flexure in Advances in Geophysics, volume 21. San Diego,
790 California, USA, pp. 51 – 86.

791 [62] Turcotte, D., & Schubert, G., 2002. Geodynamics. Cambridge University Press,
792 pp. 141–161.
793 [63] Wang, B., Chen, Y., Zhan, S., Shu, L., Faure, M., Cluzel, D., Charvet, J.,
794 Laurent-Charvet, S., 2007. Primary Carboniferous and Permian paleomagnetic
795 results from the Yili Block (NW China) and their implications on the geodynamic
796 evolution of Chinese Tianshan belt. Earth & Planetary Science Letters. 263, 288–
797 308. https://doi.org/10.1016/j.epsl.2007.08.037
798 [64] Wang, H., Liu, M., Cao, J., Shen, X., & Zhang, G., 2011. Slip rates and seismic
799 moment deficits on major active faults in mainland China. Journal of Geophysical
800 Research, 116, B02405. https://doi.org/10.1029/2010JB007821
801 [65] Wang, Q., Zhang, P.-Z., Freymueller, J.T., Bilham, R., Larson, K.M., Lai, X.,
802 You, X., Niu, Z., Wu, J., Li, Y., Liu, J., Yang, Z., & Chen, Q., 2001. Present-day
803 crustal deformation in China constrained by global positioning system
804 measurements. Science, 294, 574–577. http://dx.doi.org/10.1126/science.1063647
805 [66] Wang, L. S., Li, C., and Shi, Y. S., 1995. The distribution characteristics of heat
806 flow densities in Tarim Basin. Science in China, 38, 855–856. (in Chinese)
807 [67] Wang, S. L., Chen, Y., Charreau, J., Wei, D. T., Jia, D., 2013.
808 Tectono-stratigraphic history of the southern Junggar basin: seismic profiling
809 evidences. Terra Nova, 25, 490–495. http://dx.doi.org/10.1111/ter.12063
810 [68] Wang, X., Sun, D., Chen, F., Wang, F., & Li, Z., 2014. Cenozoic
811 paleo-environmental evolution of the Pamir–Tien Shan convergence zone.
812 Journal of Asian Earth Sciences, 80, 84–100.
813 http://dx.doi.org/10.1016/j.jseaes.2013.10.027
814 [69] Watts, A. B., 2001. Isostasy and Flexure of the Lithosphere. Cambridge
815 University Press, pp. 48–283.

816 [70] Wei, H. H., Meng, Q. R., Ding, L., & Li, Z. Y., 2013. Tertiary evolution of the
817 western Tarim Basin, northwest China: A Tectono-sedimentary response to
818 northward indentation of the Pamir salient. Tectonics, 32, 558–575.
819 http://dx.doi.org/10.1002/tect.20046
820 [71] Windley, B.F., Allen, M.B., Zhang, C., Zhao, Z.Y., & Wang, G.R., 1990.
821 Paleozoic accretion and Cenozoic deformation of the Chinese Tien Shan Range,
822 central Asia. Geology, 18, 128–131.
823 http://dx.doi.org/10.1130/0091-7613(1990)018<0128:PAACRO>2.3.CO;2
824 [72] Wickert, A, D., 2016. Open-source modular solutions for flexural isostasy: gflex
825 v1.0. Geoscientific Model Development, 9, 997–1017.
826 http://dx.doi.org/10.5194/gmd-9-997-2016
827 [73] Wright, M.H., 1996. “Direct Search Methods: Once Scorned, Now Respectable”,
828 in Numerical Analysis 1995, Proceedings of the 1995 Dundee Biennial
829 Conference in Numerical Analysis, D.F. Griffiths and G.A. Watson (Eds.),
830 Addison Wesley Longman, Harlow, UK, pp. 191–208.
831 [74] Xiao, W.J., Windley, B.F., Chen, H.L., Zhang, G.C., & Li, J.L., 2002.
832 Carboniferous-Triassic subduction and accretion in the western Kunlun, China:
833 implications for the collisional and accretionary tectonics of the northern Tibetan
834 Plateau. Geology, 30, 295-298.
835 http://dx.doi.org/10.1130/0091-7613(2002)0302.0.CO;2
836 [75] Xinjiang Bureau of Geology and Mineral Resources (Xinjiang BGMR)., 1993.
837 Regional Geology of Xinjiang. Geological Publishing House, Beijing, pp. 1-841
838 (in Chinese with English Abstract).

839 [76] Yan, F, L., Lu, H, F., Jia, D., Yu, J, M., 2003. The Meso-Cenozoic Subsidence
840 Features of Kuqa Depression, Tarim Basin. Journal of Nanjing University
841 (Natural Sciences), 39, 31–39. (in Chinese with English abstract)
842 [77] Yang, S.F., Li, Z.L., Chen, H.L., Santosh, M. & Dong, C.W., 2007. Permian
843 bimodal dyke of Tarim Basin, NW China: geochemical characteristics and
844 tectonic implications. Gondwana Research., 12(1–2), 113–120.
845 https://doi.org/10.1016/j.gr.2006.10.018
846 [78] Yang, W., Dupont-Nivet, G., Jolivet, M., Guo, Z., Bougeois, L., Bosboom, R.,
847 Zhang, Z, Y., Zhu, B., & Heilbronn, G., 2015. Magnetostratigraphic record of the
848 early evolution of the southwestern Tian Shan foreland basin (Ulugqat area),
849 interactions with Pamir indentation and India–Asia collision. Tectonophysics,
850 644, 122–137. http://dx.doi.org/10.1016/j.tecto.2015.01.003
851 [79] Yang, Y., & Liu, M., 2002. Cenozoic deformation of the Tarim plate and the
852 implications for mountain building in the Tibetan plateau and the Tian Shan.
853 Tectonics, 21, 1059. http://dx.doi.org/10.1029/2001tc001300
854 [80] Yin, A., Nie, S., Craig, P., Harrison, T.M., Ryerson, F.J., Qian, X., & Yang, G.,
855 1998. Late Cenozoic tectonic evolution of the southern Chinese Tian Shan.
856 Tectonics, 17, 1–27. http://dx.doi.org/10.1029/97TC03140
857 [81] Yin, A., 2000. Mode of Cenozoic east-west extension in Tibet suggesting a
858 common origin of rifts in Asia during the Indo-Asian collision. Journal of
859 Geophysical Research: Solid Earth, 105, 21745–21759.
860 http://dx.doi.org/10.1029/2000JB900168
861 [82] Yin, A., & Harrison, M, T., 2000. Geologic Evolution of the Himalayan-Tibetan
862 orogen. Annual Review of Earth and Planetary Sciences, 28, 211–280.
863 http://dx.doi.org/10.1146/annurev.earth.28.1.211

[83] Yin, A., Rumelhart, P., Butler, R., Cowgill, E., Harrison, T., Foster, D., Ingersoll, R., Zhang, Q., Zhou, X., Wang, X., Hanson, A., & Raza, A., 2002. Tectonic history of the Altyn Tagh fault system in northern Tibet inferred from Cenozoic sedimentation. Geological Society of America Bulletin, 114, 1257–1295. http://dx.doi.org/10.1130/0016-7606(2002)114<1257:thotat>2.0.co;2

[84] Yu, X. J., Guo, Z. J., & Fu, S. T., 2015. Endorheic or exorheic: differential isostatic effects of Cenozoic sediments on the elevations of the cratonic basins around the Tibetan Plateau. Terra Nova, 27, 21–27. http://dx.doi.org/10.1111/ter.12126

[85] Yu, Y., Tang, L., Yang, W., Huang, T., Qiu, N., & Li, W., 2014. Salt structures and hydrocarbon accumulations in the Tarim Basin, northwest China. American Association of Petroleum Geologists Bulletin, 98, 135–159. http://dx.doi.org/10.1306/05301311156

[86] Zhang, S., Huang, Z., Zhu, H., 2004. Phanerozoic stratigraphy in covered area of Tarim Basin. Petroleum Industry Press, Beijing, 1–300. (in Chinese)

[87] Zhang, T., Fang, X., Song, C., Appel, E., & Wang, Y., 2014. Cenozoic tectonic deformation and uplift of the south Tian Shan: implications from magnetostratigraphy and balanced cross-section restoration of the Kuqa depression. Tectonophysics, 628, 172–187. http://dx.doi.org/10.1016/j.tecto.2014.04.044

[88] Zhao, J. M., Liu, G., Lu, Z., Zhang, X., & Zhao, G., 2003. Lithospheric structure and dynamic processes of the Tian Shan orogenic belt and the Junggar basin. Tectonophysics, 376, 199–239. http://dx.doi.org/10.1016/j.tecto.2003.07.001

[89] Zheng, G., Wang, H., Wright, T. J., Lou, Y., Zhang, R., Zhang, Wang, W., Shi, C., Huang, J. F., Wei, N., 2017. Crustal deformation in the India-Eurasia collision

889 zone from 25 years of GPS measurements. Journal of Geophysical Research:
890 Solid Earth, 122, 9290–9312. http://dx.doi.org/10.1002/2017JB014465
891 [90] Zubovich, A. V., Wang, X., Scherba, Y. G., Schelochkov, G. G., Reilinger, R., &
892 Reigber, C., Mosienko, O., Molnar, P., Michajljow, W., Makarov, V, I., Li, J.,
893 Kuzikov, S, I., Herring, T, A., Hamburger, M, W., Hager, B, H., Dang, Y. M.,
894 Bragin, V, D., Beisenbaev, R, T., 2010. GPS velocity field for the Tien Shan and
895 surrounding regions. Tectonics, 29, 10–1029.
896 http://dx.doi.org/10.1029/2010TC002772
897

Figures

Figure 1

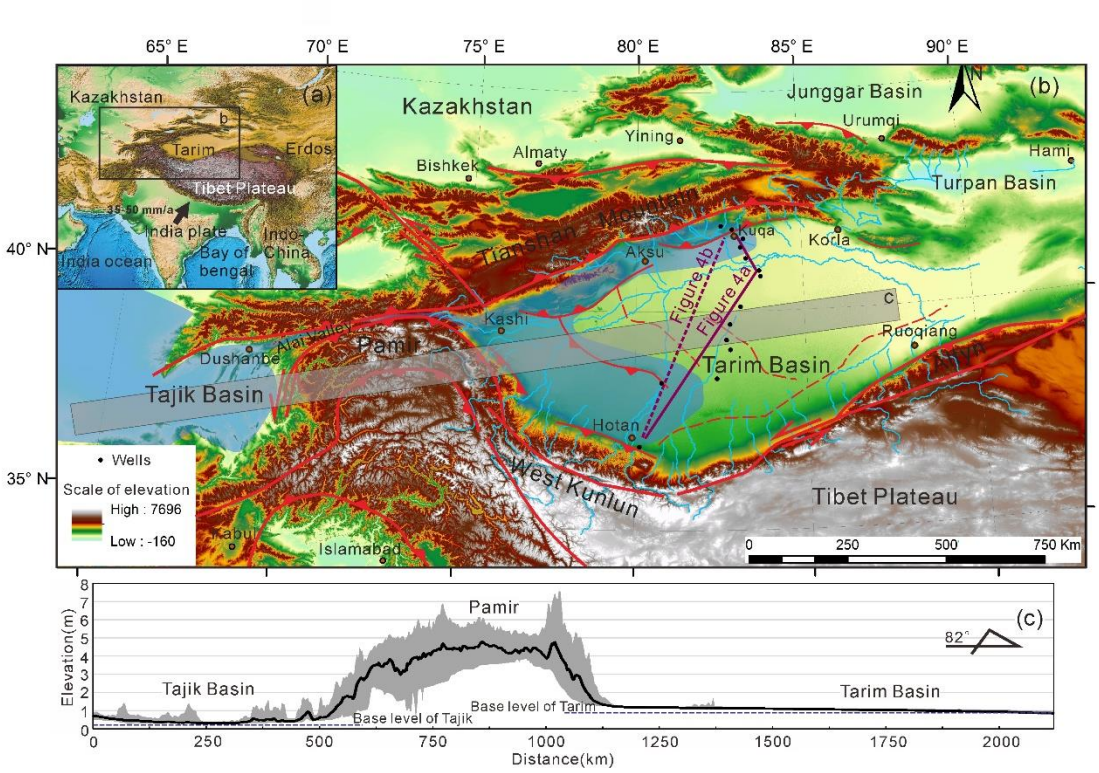

Figure 1. (a) The Tarim Basin in the India-Asia collisional system. The movement of the Indian plate is from Wang et al. (2001). (b) DEM map of the Tarim basin and adjacent area with major faults. The faults are drawn from Yin (2000) and Yin et al. (2002). Drainage network in the basin derived from DEM is marked in blue. The solid purple line is the north-northeast trending seismic profile; the purple dashed line is the projected profile. Locations of wells are marked by black dots. The blue shadow denotes the largest extent of marine incursion into the Tarim Basin during the Paleogene (Wang et al. 2014; Yang et al. 2015; Carrapa et al. 2015). (c) A topographic swath across the Tajik Basin, the Pamir plateau and Tarim Basin (for location see Fig. 1b).

Figure 2

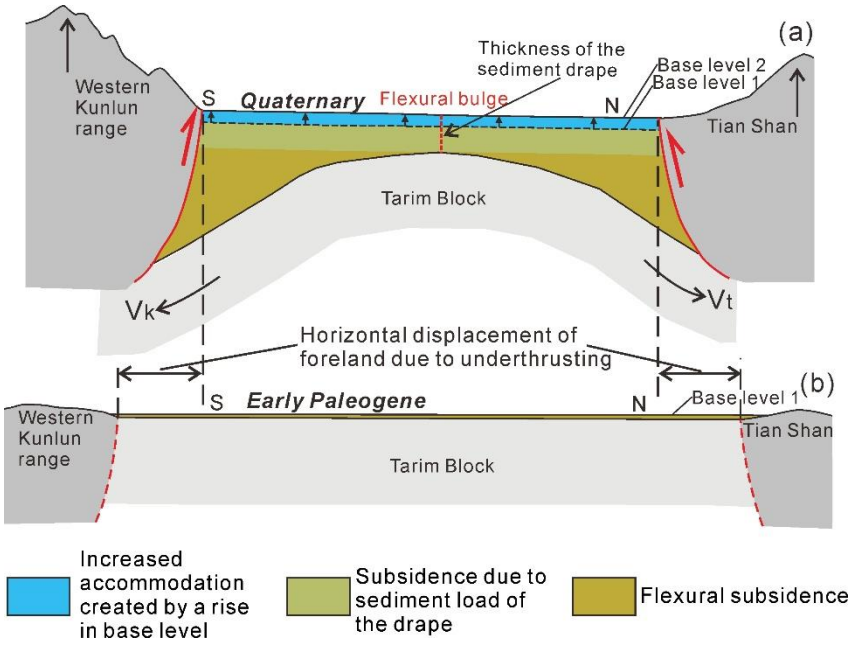

Figure 2. Sketch of the evolution of the flexural subsidence and the sediment drape in the Cenozoic Tarim Basin. The finite plate model indicates the flexural subsidence in the basin with finite width is driven by the growth of mountain topography on either side. The sediment drape comprises the increased accommodation due to a rise in base level and the subsidence due to sediment load of the drape. The basement subsidence comprises flexural subsidence and subsidence due to the sediment load of the drape. The length of the red vertical dashed line in the flexural bulge represents the thickness of the drape. The V_K and V_T are the underthrusting rates of the Tarim lithosphere beneath the western Kunlun range and the Tian Shan, respectively.

Figure 3

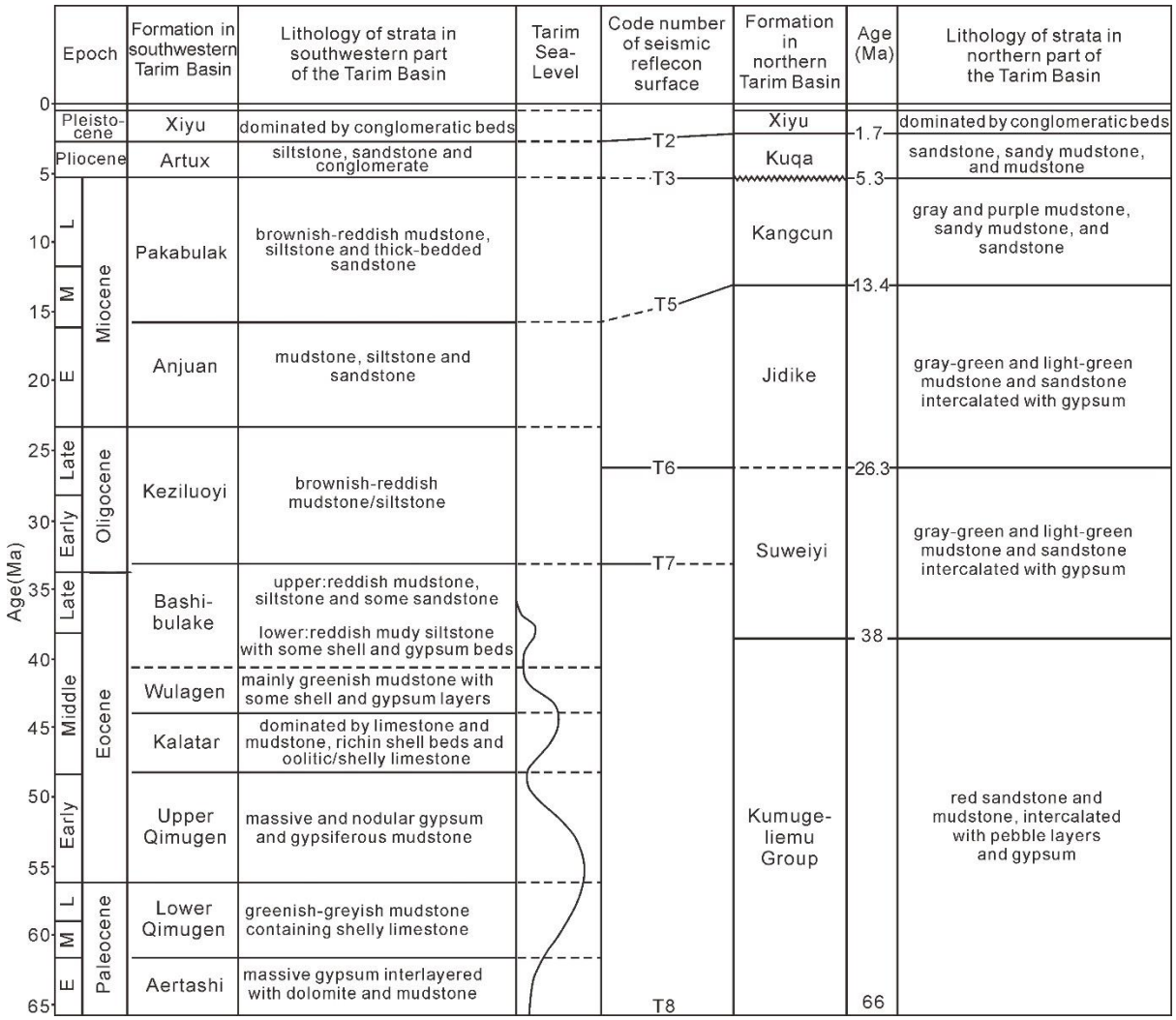

Figure 3. The simplified regional lithostratigraphic framework correlation of the southwestern and northern depressions of the Tarim Basin, after Bosboom et al. (2014b). The lithology of each formation is summarized from Zhang et al. (2004). The ages of formations in the southwestern depression were estimated based on works about calcareous nannofossils, bivalves, ostracods, dinoflagellate cysts and benthic foraminifera and paleomagnetostratigraphy (Bosboom et al., 2011; Bosboom et al., 2014a). The ages of formations in the northern depression are constrained by paleomagnetostratigraphic studies (Huang et al., 2006; Charreau et al., 2009; Zhang et al., 2014). The approximately relative changes in sea level of each transgression are in accordance with the reported eastward extent of each incursion into the basin (Bosboom et al., 2014a; 2014b).

Figure 4

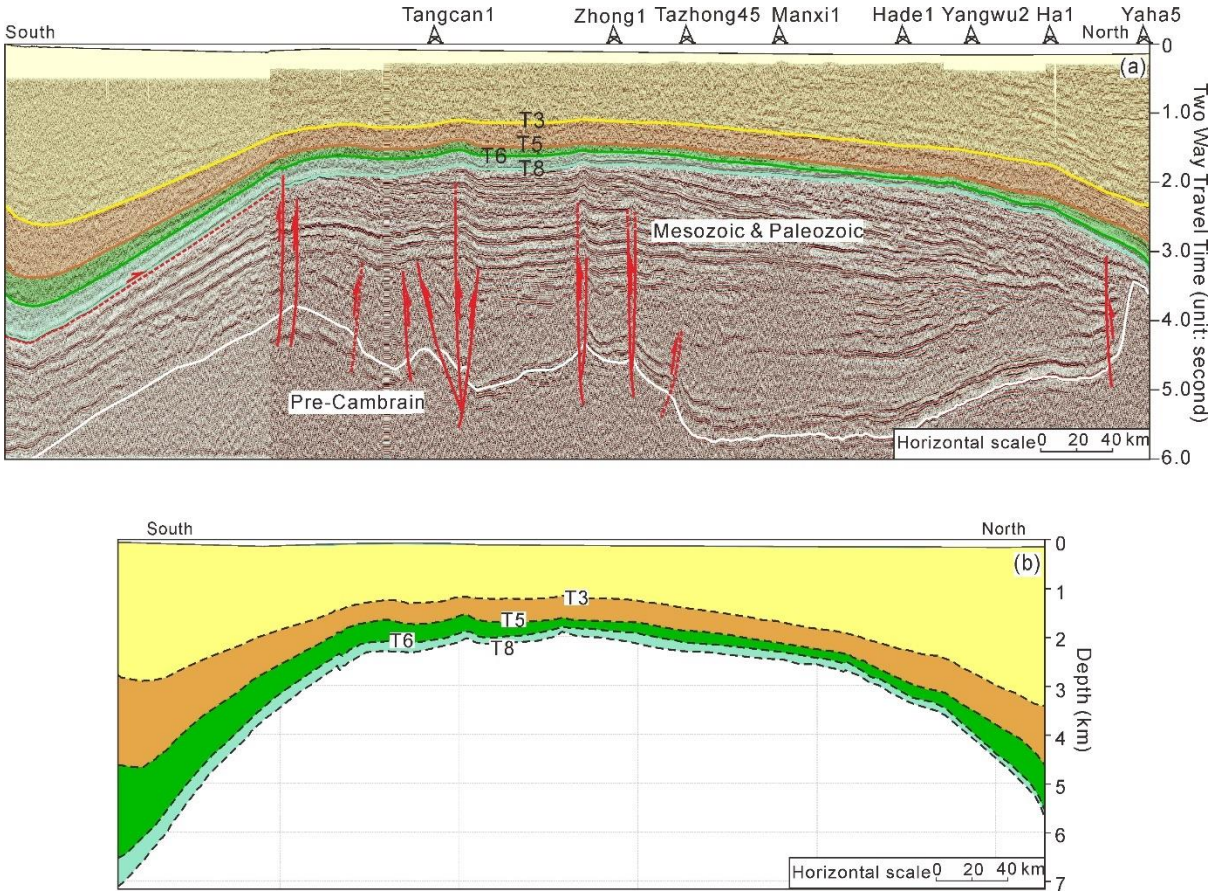

Figure 4. (a) The interpreted north-northeast trending seismic profile across the Tarim Basin. See Fig. 1 for its location. Vertical exaggeration is ~18X. Cenozoic strata are divided by the seismic reflectors of T3, T5, T6, and T8. The bottom of the Phanerozoic strata is marked by the white dashed line. These boundaries and faults are interpreted from well logging data near the profile and interpretations of other seismic reflection profiles across the Tarim Basin from previous publications (Jiang, 2014; Yu et al., 2014; Li et al., 2015). (b) The projected depth section of Fig. 4a. See Fig. 1b for its location.

Figure 5

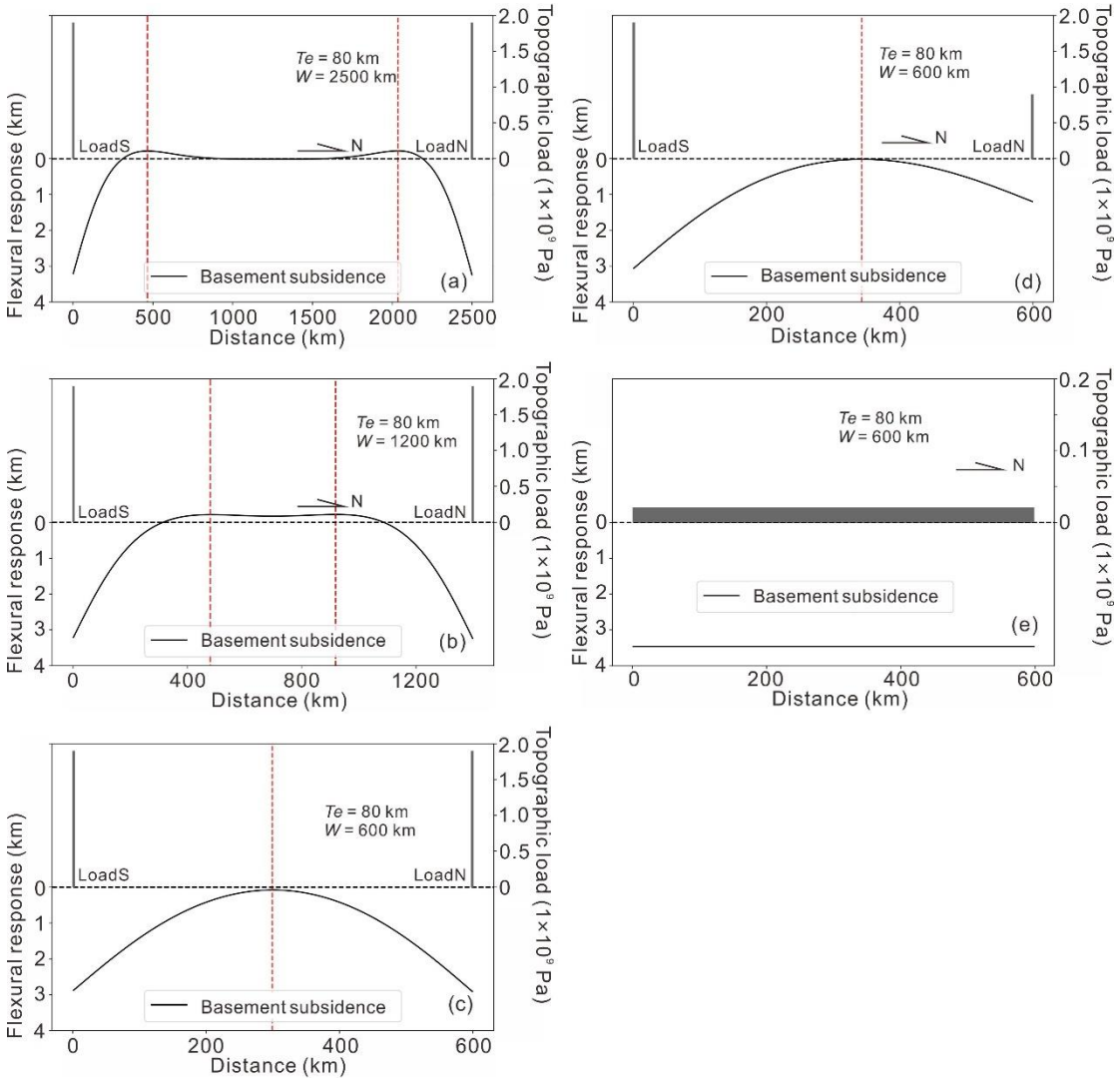

Figure 5. (a), (b) & (c) Effects of symmetric loadings on the northern and southern margins of the finite plate, with W of 2500 km, 1200 km and 600 km. (d) Effects of asymmetric loadings on the northern and southern margins, with W of 600 km. (e) The application of a uniform drape across the finite plate. The grey histograms in (a), (b), (c) and (d) represent the topographic loads with 2 km width on the margins of the plate. The grey filled rectangle in (e) represents the uniform topographic load imposed onto the plate. The red dashed lines mark locations of the flexural bulges.

Figure 6

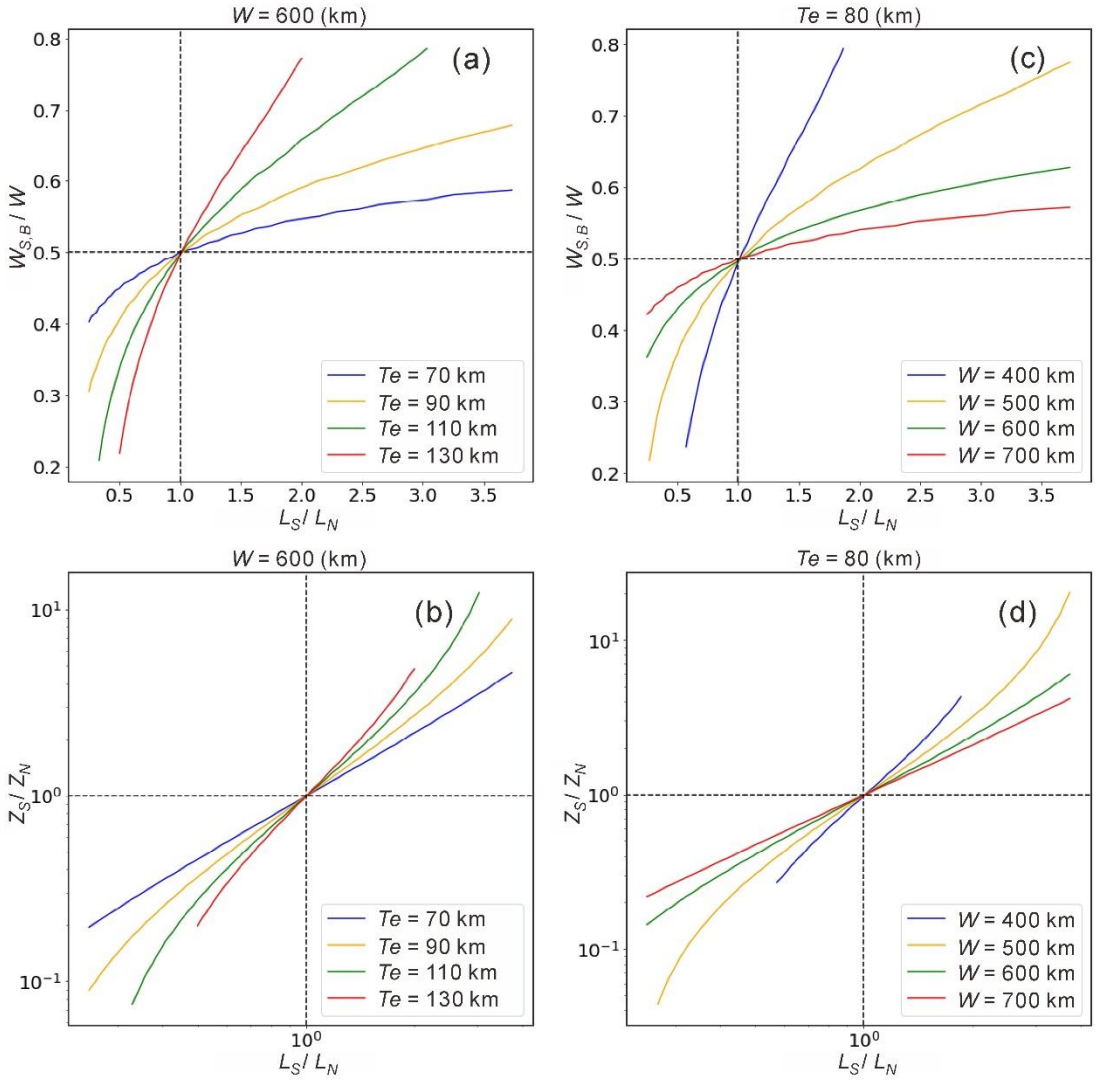

Figure 6. (a) and (c) The relation between positions of the flexural bulge ($W_{S,B}/W$) and relative loads both sides of the plate (L_S/L_N). (b) and (d) The relation between Z_S/Z_N and L_S/L_N. The left column shows the impact of varying Te. The right column shows the impact of varying basin width W. $W_{S,B}$ is the distance from the southern boundary of the basin to the flexural bulge. Z_S and Z_N are maximum subsidence in the south and north depressions, respectively.

963 **Figure 7**

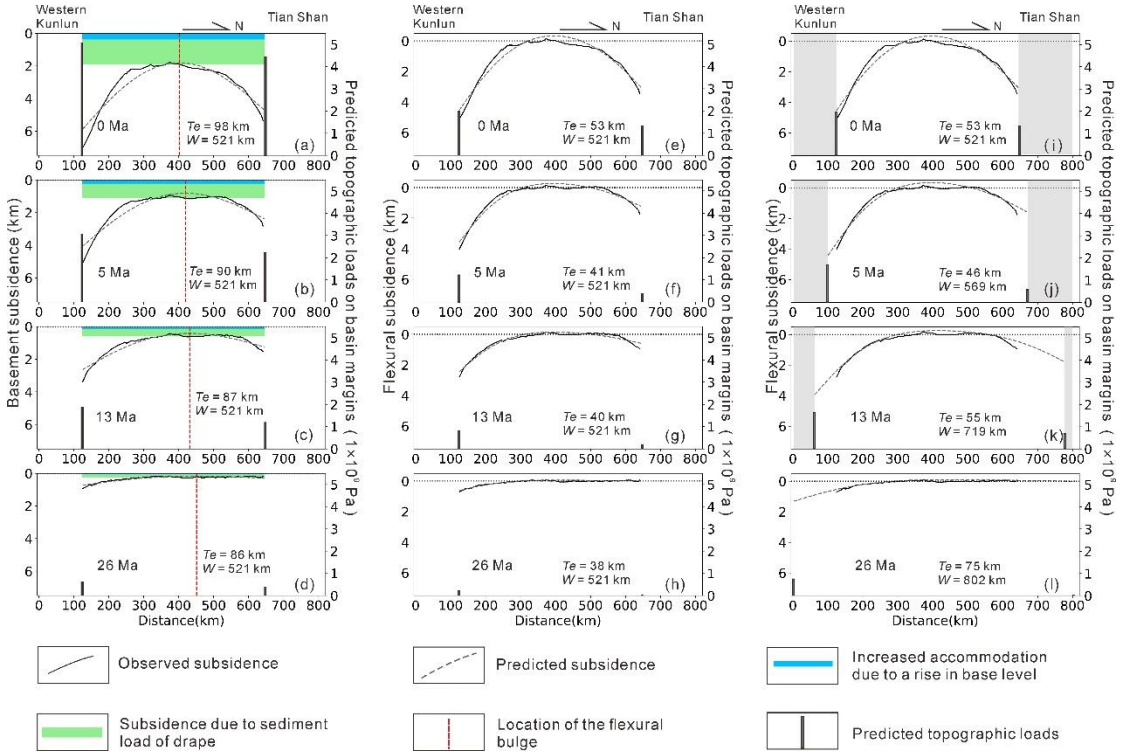

964

965 **Figure 7**. (a), (b), (c) & (d) Modelled basement subsidence profiles across the Tarim
966 Basin at four moments. (e), (f), (g) & (h) Modelled flexural subsidence profiles with a
967 fixed basin width at four moments. (i), (j), (k), (l) Modelled flexural subsidence
968 profiles with decreasing basin widths at four moments. The southern margin of the
969 Tarim Basin at ~26 Ma is set to the zero point of the abscissa in the reference system.
970 The black histograms represent the predicted topographic loads (with 2 km width) of
971 the western Kunlun range and the Tian Shan on the southern and northern margins,
972 respectively. Grey shadows in (i), (j), (k), and (l) denote horizontal underthrusting of
973 the Tarim lithosphere.

974 **Figure 8**

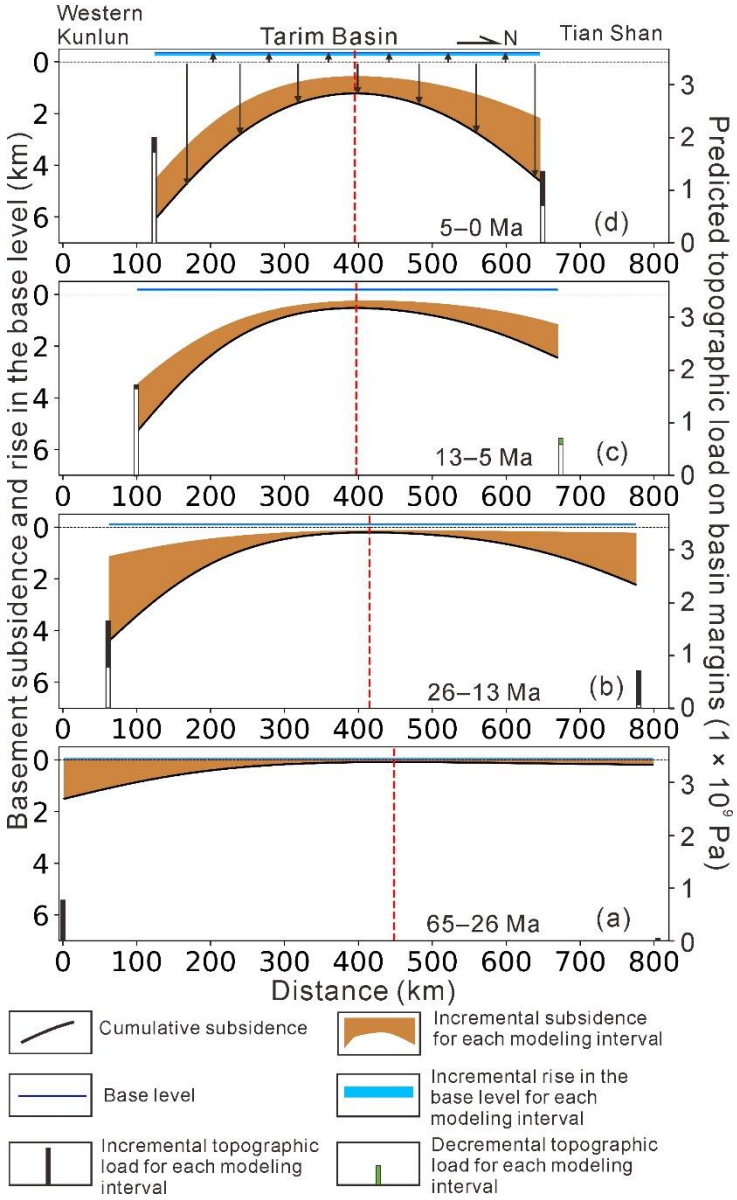

975

976 **Figure 8**. Modelled evolution of the basement subsidence and rise of the base level in
977 the Tarim Basin with decreasing basin width. The increased accommodation due to a
978 rise in the base level is above the horizontal datum because it is formed due to the
979 uplift of the topography rather than the subsidence in the basin. The histograms
980 represent the predicted topographic loads (with 2 km width) of the western Kunlun
981 range and the Tian Shan on the southern and northern margins, respectively.

Figure 9

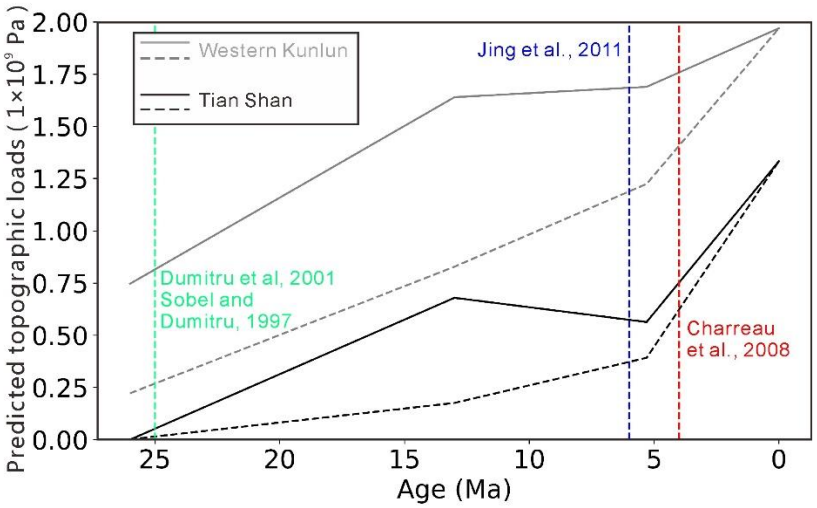

Figure 9. Summary of the predicted topographic loads of the western Kunlun range and the Tian Shan based on the subsidence modelling. The black and grey solid lines denote the topographic loads of the western Kunlun range and the Tian Shan under decreasing W. The black and grey dashed lines denote the topographic loads of the western Kunlun range and the Tian Shan under the fixed W. The green vertical line marks the times of the initial uplifts of the Tian Shan (Dumitru et al., 2001) and the western Kunlun range (Sobel and Dumitru, 1997) based on low-temperature thermochronological works. The times of the increases of the sediments accumulation rate in the piedmonts of the Tian Shan at ~6 Ma and ~4 Ma (Charreau et al., 2008; Jing et al., 2011) are marked as the blue and red vertical lines, respectively.

995 **Tables**

996 **Table 1**. Lithological and decompaction parameters used in backstripping (Sclater
997 and Christie, 1980).

Lithology	Compaction decay length $C*$ (10^5/cm^{-1})	Initial porosity φ_0	Sediment grain density ρ_S (g cm^{-3})
Sandstone	0.27	0.49	2.65
Shale stone	0.51	0.63	2.72
Limestone	0.71	0.7	2.71
Shaly sand	0.39	0.56	2.68

998

999 **Table 2**. Horizontal displacements of the forelands due to underthrusting and
1000 historical basin widths (Li et al., 2019).

Time / Ma	Horizontal displacement of the foreland of the western Kunlun range / km	Horizontal displacement of the foreland of the Tian Shan / km	The width of the Tarim Basin / km
26	0	0	802
13	62	21	719
5	100	133	569
0	124	157	521

1001

1002 **Table 3**. Thicknesses of the sediment drapes and the cumulative increased
1003 accommodations due to rises in the base level.

Time / Ma	Thickness of the drape / m	Increased accommodation due to a rise in the base level

		/ m
26	230±30	43±15
13	624±65	117±35
5	1123±120	210±55
0	1910±200	356±80

Table 4. Predicted topographic loads of the western Kunlun range and the Tian Shan under fixed and decreasing basin widths.

Time / Ma	Western Kunlun range (fixed W) / MPa	Western Kunlun range (decreasing W) / MPa	Tian Shan (fixed W) / MPa	Tian Shan (decreasing W) / MPa
26	221	746	2	4
13	828	1640	176	679
5	1225	1690	392	563
0	1970	1970	1333	1333